coatings

Article

First-Principles Analysis of Phase Stability and Transformation Suppression for Hydrogen-Doped Alumina

Kun Lv [1], Shiyang Sun [1,*], Bo Yuan [1], Xiaofeng Guo [1,*], Weiao Song [1] and Andrei A. Boiko [2]

[1] School of Mechanical Engineering, Inner Mongolia University of Science and Technology, Baotou 014010, China; lvkun@stu.imust.edu.cn (K.L.); bo.yuan@imust.edu.cn (B.Y.); 19862520173@163.com (W.S.)
[2] Research Laboratory "Technical Ceramics and Nanomaterials", Sukhoi State Technical University of Gomel, 48 Prospect Octiabria, 246746 Gomel, Belarus; boiko@gstu.by
* Correspondence: sunshy@imust.edu.cn (S.S.); guoxiaofeng@imust.edu.cn (X.G.)

Abstract: Thermally grown oxide (TGO) layers—primarily alumina (Al_2O_3)—provide oxidation resistance and high-temperature protection for thermal barrier coatings. However, during their service in humid and hot environments, water vapor accelerates TGO degradation by stabilizing metastable alumina phases (e.g., θ-Al_2O_3) and inhibiting their transformation to the thermodynamically stable α-Al_2O_3, a phenomenon which has been shown in numerous experimental studies. However, the microscopic mechanisms by which water vapor affects the phase stability and transformation of alumina remain unresolved. This study employs first-principles calculations to investigate hydrogen's role in altering vacancy formation, aggregation, and atomic migration in θ- and α-Al_2O_3. The results reveal that hydrogen incorporation reduces the formation energies for aluminum and oxygen vacancies by up to 40%, promoting defect generation and clustering; increases aluminum migration barriers by 25–30% while lowering oxygen migration barriers by 15–20%, creating asymmetric diffusion kinetics; and stabilizes oxygen-deficient sublattices, disrupting the structural reorganization required for θ- to α-Al_2O_3 transitions. These effects collectively sustain metastable θ-Al_2O_3 growth and delay phase stabilization. By linking hydrogen-induced defect dynamics to macroscopic coating degradation, this work provides atomic-scale insights for designing moisture-resistant thermal barrier coatings through the targeted inhibition of vacancy-mediated pathways.

Keywords: alumina oxide; phase transformation; hydrogen suppression; first-principles calculations

Academic Editors: Manuel Miguel Jordan-Vidal and María Belén Almendro-Candel

Received: 27 March 2025
Revised: 28 April 2025
Accepted: 30 April 2025
Published: 2 May 2025

Citation: Lv, K.; Sun, S.; Yuan, B.; Guo, X.; Song, W.; Boiko, A.A. First-Principles Analysis of Phase Stability and Transformation Suppression for Hydrogen-Doped Alumina. *Coatings* **2025**, *15*, 545. https://doi.org/10.3390/coatings15050545

1. Introduction

Thermal barrier coatings (TBCs) are critical for protecting hot-section components of aero-engines, including turbine blades, combustion chambers, and nozzles, due to their exceptional thermal insulation, oxidation resistance, and corrosion protection [1–5]. A typical TBC system comprises three layers: a ceramic topcoat, a metallic bond coat (typically MCrAlY), and a superalloy substrate [1–5]. During service, oxygen permeates the top coat layer and reacts with metallic elements in the bond coat, forming thermally grown oxide (TGO) primarily composed of alumina (Al_2O_3) [1–3].

The ideal TGO consists of a dense, fast-growing α-Al_2O_3 phase with high thermodynamic stability, which effectively inhibits oxygen diffusion and enhances oxidation resistance [4,5]. However, under operational conditions involving thermal cycling and oxidizing environments, metastable alumina phases (e.g., γ-, η-, δ-, and θ-Al_2O_3) often nucleate prior to α-Al_2O_3 formation due to gradients in oxygen partial pressure, temperature, and stress [6–10]. These metastable polymorphs exhibit distinct physical properties, with γ- and θ-Al_2O_3 growing up to two orders of magnitude faster than α-Al_2O_3 [11–15]. Consequently, the phase stability of α-Al_2O_3 governs the oxidation kinetics, stress evolution, and long-term performance of TBC systems.

Extensive research over the past two decades has elucidated the oxidation behavior of bond coat layers. At temperatures below 1200 °C, metastable γ- or θ-Al_2O_3 typically forms initially due to kinetic favorability, subsequently transforming to α-Al_2O_3 through prolonged oxidation [4–10]. This phase transition is accompanied by volumetric shrinkage and defect generation, which accelerate ionic diffusion, induce growth stresses, and promote interfacial microcracking [16–18]. The metastable-to-stable phase evolution thus critically influences TGO morphology, mechanical integrity, and TBC lifespan. Recent studies highlight the role of metastable alumina in interfacial degradation. For instance, Zhang et al. [19] investigated γ-Al_2O_3/Al interfacial properties using first-principles calculations, while Sakakibara et al. [20] observed transient η- and θ-Al_2O_3 nanoparticles via transmission electron microscopy prior to α-Al_2O_3 crystallization. Despite these advances, the energy landscape governing θ- to α-Al_2O_3 transitions remains poorly characterized.

In water vapor-enriched gas turbine environments, hydrogen (H) accelerates TBC degradation by stabilizing metastable alumina and inhibiting α-Al_2O_3 formation [21,22]. The proposed mechanisms include enhanced cation diffusion [23], altered Al/O ion mobility [24], and hydroxyl-induced vacancy formation [25–27]. For example, Yan et al. [25] suggested that dissociated protons from H_2O disrupt oxide electroneutrality, increasing cation vacancy concentrations and suppressing θ- to α-Al_2O_3 transitions. Similarly, Zhu et al. [26] and Cheng et al. [27] attributed prolonged metastable phase growth to water-vapor-promoted defect density and atomic diffusion. However, the atomistic mechanisms underlying these phenomena remain unresolved.

The θ- to α-Al_2O_3 transition is hypothesized to involve either diffusional restructuring [28] or cooperative oxygen sublattice shear combined with Al^{3+} migration [29]. Bagwell et al. [28] demonstrated that α-Al_2O_3 nucleation proceeds via diffusion rather than shear-driven reconfiguration. In contrast, Huang et al. [29] proposed a simultaneous shear–migration mechanism based on first-principles calculations. Despite these insights, the influence of water vapor on phase transition energetics and kinetics lacks a unified explanation.

Numerous studies have shown that water vapor accelerates TGO degradation, yet the microscopic mechanisms by which it affects the phase stability and transformation of alumina remain unclear. This study aims to elucidate the microscopic mechanisms by which water vapor influences the phase stability and transformation of alumina. To achieve these objectives, we employed first-principles calculations to investigate the impact of hydrogen on vacancy formation, aggregation, and atomic migration in θ- and α-Al_2O_3. These findings enhance the fundamental understanding of oxidation mechanisms and provide theoretical guidance for the design of more durable TBC systems.

2. Materials and Methods of Research

The α-Al_2O_3 crystal (space group R-3c; trigonal system) adopts a close-packed configuration with lattice constants $a = b = 0.4759$ nm and $c = 1.291$ nm, containing 30 atoms per unit cell [30–32]. As shown in Figure 1a, a (3 × 3 × 1) supercell expansion of the α-Al_2O_3 protocell yielded a 270-atom model with a hydrogen concentration of 0.37 at%. In α-Al_2O_3, O and Al atoms occupy single crystallographic sites, necessitating the consideration of only two vacancy configurations—octahedral Al vacancies ($V_{Al\text{-}oct}$) and O vacancies (V_O). To construct these defects, one Al atom was removed from both pristine and hydrogen-doped α-Al_2O_3 to form $V_{Al\text{-}oct}$, while one O atom was removed to generate V_O. Structural optimization was performed to stabilize the models. In addition, θ-Al_2O_3

exhibits monoclinic symmetry (space group C2/m) with lattice parameters a = 11.9 Å, b = 2.9 Å, and c = 5.56 Å, comprising 20 atoms per unit cell (four formula units) with all atoms occupying 4i Wyckoff positions [33]. A (1 × 4 × 2) supercell expansion (Figure 1b) produced a 160-atom model with 0.625 at% hydrogen. In θ-Al_2O_3, O atoms occupy a single equivalent site, requiring only one V_O configuration. Al atoms reside in tetrahedral and octahedral interstitial positions, leading to two distinct Al vacancy models—tetrahedral ($V_{Al\text{-}tet}$) and octahedral ($V_{Al\text{-}oct}$). These defects were modeled by removing one tetrahedral or octahedral Al atom from pristine and hydrogen-doped θ-Al_2O_3, respectively, followed by structural optimization.

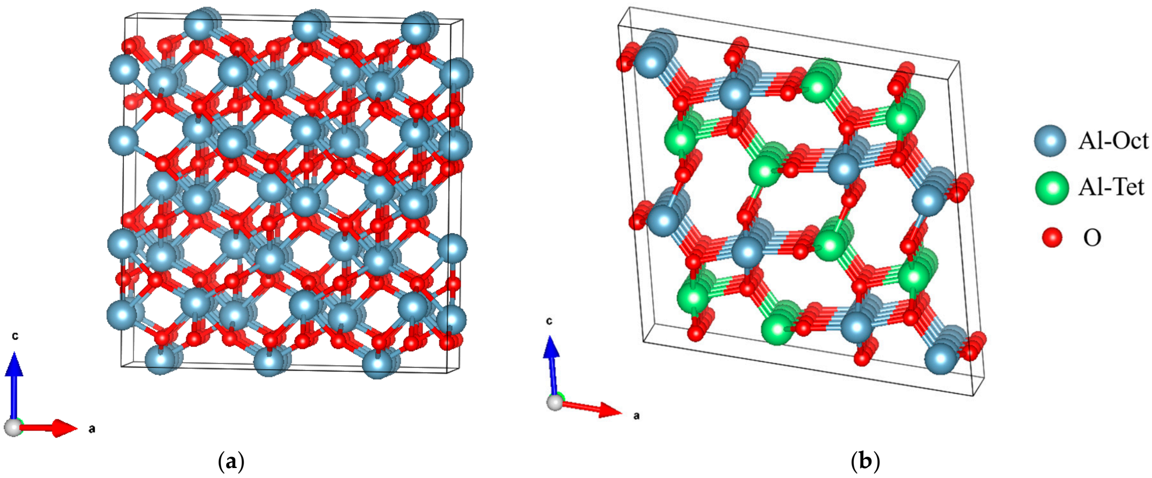

Figure 1. (**a**) A (3 × 3 × 1) α-Al_2O_3 supercell; (**b**) a (1 × 4 × 2) θ-Al_2O_3 supercell. Al atoms in tetrahedral (green) and octahedral (blue) coordination are distinguished, while O atoms are shown in red.

First-principles calculations were performed to investigate vacancy formation, aggregation, and atomic migration, as well as hydrogen doping effects on alumina growth with phase transformation. Large supercells with low defect concentrations (≤0.625 at%) were employed to minimize defect interactions and reflect local structural properties. All calculations utilized the VASP software package with the PAW-PBE pseudopotential and generalized gradient approximation (GGA) for exchange-correlation. The H pseudopotential (PAW_PBE H 15Jun2001) was selected to model neutral hydrogen atoms, which is consistent with prior studies of H diffusion in alumina [34,35]. A 3 × 3 × 3 Monkhorst-Pack k-point grid, a plane-wave cutoff energy of 500 eV, and convergence criteria of 10^{-4} eV (electronic) and 10^{-5} eV (total energy) were applied. Structural optimizations ensured force convergence below 0.001 eV/Å. This approach accurately describes core–electron interactions and defect-related electronic structures, as well as enabling the precise evaluation of key properties including vacancy formation energies and migration barriers. This ensures both reliable structural predictions and computational efficiency for complex oxide systems such as alumina.

In detail, the formulae assessing the vacancy formation difference (δE) between H-free and H-doped systems, i.e., E_{form} and E^H_{form} are as follows:

$$E_{form} = E_V + \varepsilon - E_{pr} \quad (1)$$

$$E^H_{form} = E^H_V + \varepsilon - E^H_{pr} \quad (2)$$

and

$$\delta E = E^H_{form} - E_{form} \quad (3)$$

In Equations (1)–(3), E_V and E_V^H represent the total energy for the defective H-free and H-doped Al_2O_3 systems, respectively. E_{pr} and E_{pr}^H represent the total energy for the pristine H-free and H-doped Al_2O_3 systems, respectively. ε represents the chemical potential of the removed atom (Al or O) in its standard state. Furthermore, the vacancy aggregation energy (ΔE) is defined as the difference between the double vacancy and the two separated vacancy energies, as follows:

$$\Delta E = E_{2V}^D - E_{2V}^S \quad (4)$$

where E_{2V}^D and E_{2V}^S represent the total energy of the system with two vacancies aggregated as nearest neighbors on the dense row surface and the total energy of the system with two isolated vacancies (separated beyond nearest-neighbor distances), respectively. It is seen that $\Delta E < 0$ indicates thermodynamically favorable vacancy aggregation, while $\Delta E > 0$ suggests mutual repulsion.

For atomic diffusion studies, adjacent Al/O atom pairs in equivalent lattice planes were selected. A vacancy was created by removing one atom, while the neighboring site remained either pristine or hydrogen-doped. The final state for diffusion was generated by swapping the vacancy position with the retained atom, followed by structural optimization. Diffusion pathways were determined using the climbing image nudged elastic band (CI-NEB) method. Prior to pathway interpolation, the Variational Transition State Theory script was employed to verify the geometric similarity between optimized initial and final states, before validating the interpolation process by ensuring the continuity of atomic trajectories, finally confirming force convergence (-0.03 eV/Å) at all intermediate images.

3. Results and Discussion

3.1. Mechanical Property Validation

The mechanical properties of α-Al_2O_3 and θ-Al_2O_3 base cells (Section 2) were evaluated, including bulk modulus, shear modulus, and Young's modulus. As summarized in Table 1, the calculated values for α-Al_2O_3 are 223.26 GPa, 165.75 GPa, and 399.56 GPa, respectively, which are consistent with prior computational results [36]. For θ-Al_2O_3, the corresponding values (201.74 GPa, 142.67 GPa, and 343.35 GPa) exhibit minimal deviations of 1.35%, 0.68%, and 1.16% from the reference data [36]. These agreements validate the structural accuracy of the α-Al_2O_3 and θ-Al_2O_3 models, providing a reliable foundation for defect and atomic migration studies in Sections 3.2–3.4.

Table 1. Bulk modulus, shear modulus, and Young's modulus of crystalline cells.

Phase		Bulk Modulus (GPa)	Shear Modulus (GPa)	Young's Modulus (GPa)
α-Al_2O_3	Present model	223.26	165.75	399.56
	Reference	220.63 [36]	162.28 [36]	390.98 [36]
θ-Al_2O_3	Present model	201.74	142.67	343.35
	Reference	199.04 [36]	143.65 [36]	347.38 [36]

3.2. Vacancy Formation and Lattice Distortion

In alumina crystals, vacancies arise when atomic vibrational amplitudes exceed critical thresholds, displacing atoms from their lattice sites and inducing local distortions. Water vapor-derived H protons further influence these distortions by interacting with vacancy defects. Figures 2 and 3 illustrate the optimized supercell models of α-Al_2O_3 and θ-Al_2O_3 doped with H protons. In both phases, H protons localize near aluminum vacancies (V_{Al}), while occupying oxygen vacancy (V_O) sites. Structural optimization reveals that V_{Al} and V_O induce distinct lattice distortions, which are modulated by H incorporation.

For α-Al_2O_3 (Figure 2), the intrinsic V_O and octahedral V_{Al-oct} formation energies are 6.73 eV and 12.01 eV, respectively, matching previous calculations (see Table 2, Refs [37,38]). Upon H doping, these energies decrease to 4.56 eV (V_O) and 6.75 eV (V_{Al-oct}), corresponding to relative defect formation energies of −2.17 eV and −5.26 eV. Figure 2 demonstrates that intrinsic V_{Al-oct} causes the outward displacement of octahedral O atoms, whereas H doping mitigates inward shifts of the nearest-neighbor O atoms. Similarly, intrinsic V_O promotes the inward aggregation of diagonally coordinated Al atoms, while H incorporation suppresses this effect. These results indicate that H protons reduce the lattice distortions associated with V_{Al-oct} and V_O, thereby lowering their formation energies.

Table 2. Vacancy generation energies for H-doped and -undoped α-Al_2O_3 and θ-Al_2O_3.

Phase	Vacancy	E_{form}/eV References	E_{form}/eV Present Model	E^H_{form}/eV Present Model	δE/eV
α-Al_2O_3	V_O	6.80 [37,38]	6.73	4.56	−2.17
	$V_{Al\text{-}oct}$	12.13 [37,38]	12.01	6.75	−5.26
θ-Al_2O_3	V_O	6.20 [39]	6.11	3.29	−2.82
	$V_{Al\text{-}oct}$	-	12.51	5.91	−6.60
	$V_{Al\text{-}tet}$	-	12.09	5.14	−6.95

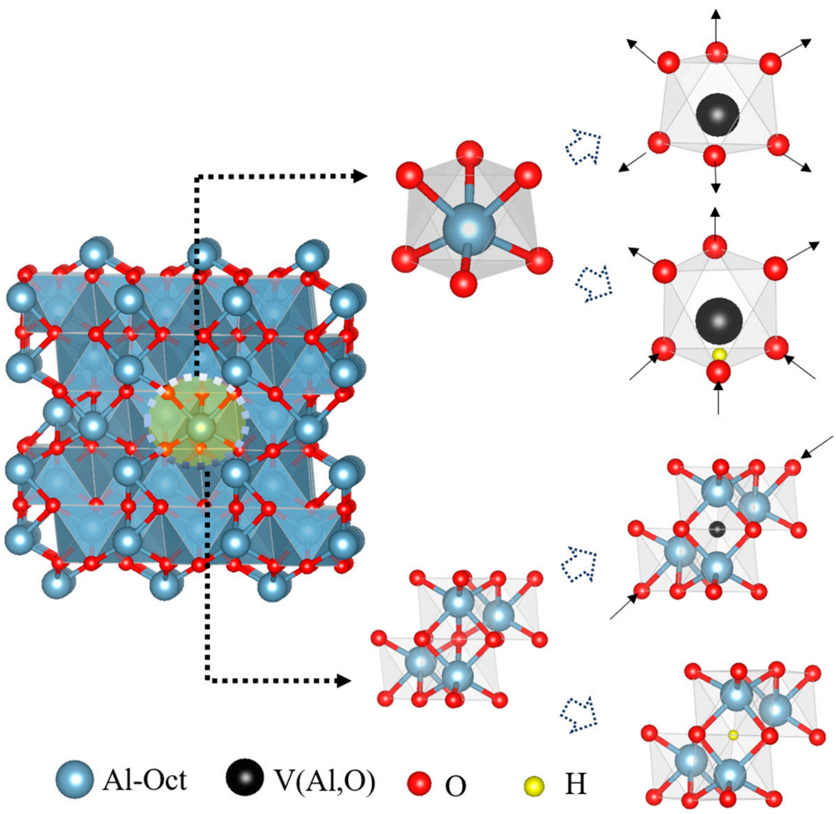

Figure 2. Atomic structure of α-Al_2O_3, highlighting octahedrally coordinated Al atoms (blue), the oxygen sublattice (red), and H atoms (yellow). Black arrows indicate lattice distortion trends.

In θ-Al_2O_3 (Figure 3), intrinsic V_O, V_{Al-oct}, and tetrahedral V_{Al-tet} exhibit formation energies of 6.11 eV, 12.51 eV, and 12.09 eV, respectively, aligning with reported V_O values (6.20 eV) [39]. H doping reduces these energies to 3.29 eV (V_O), 5.91 eV (V_{Al-oct}), and 5.14 eV (V_{Al-tet}), with relative defect formation energies of −2.82 eV, −6.60 eV, and −6.95 eV. Figure 3 shows that intrinsic V_{Al-tet} and V_{Al-oct} induce outward O displacements, while H incorporation alters the displacement directions of the adjacent O atoms. For V_O, intrinsic vacancies cause the inward aggregation of tetrahedral Al atoms and outward shifts of octahedral Al atoms; H doping counteracts the former and enhances the latter. These structural changes weaken Al-O bonding constraints near V_{Al-tet}, V_{Al-oct}, and V_O, mirroring the H-induced reduction in vacancy formation energies observed in α-Al_2O_3.

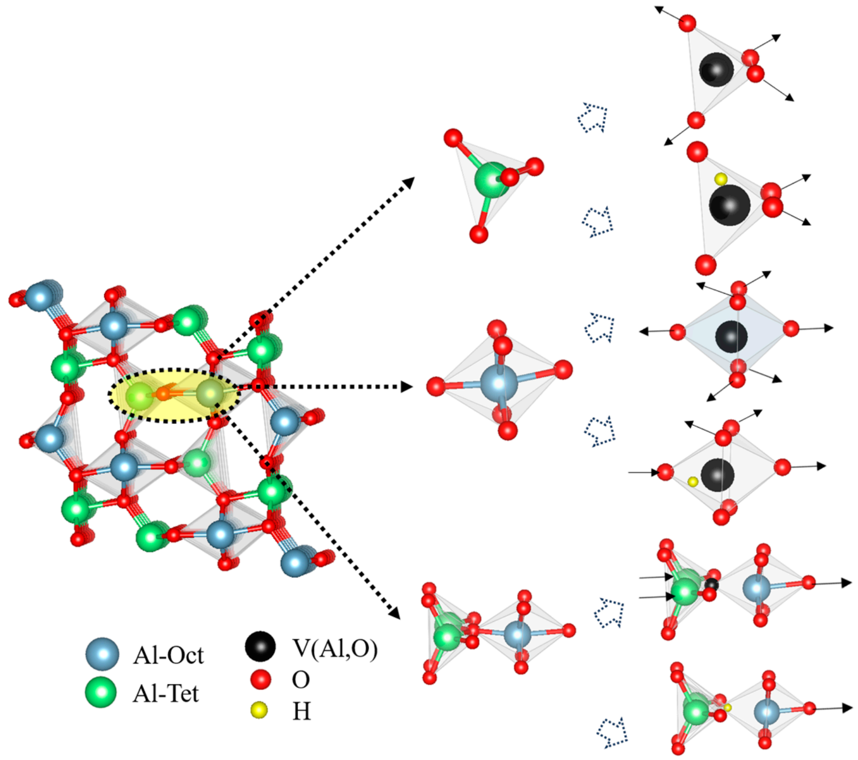

Figure 3. Atomic structure of θ-Al_2O_3, showing tetrahedrally (green) and octahedrally (blue) coordinated Al atoms, the oxygen sublattice (red), and H atoms (yellow). Black arrows denote lattice distortion trends.

3.3. Vacancy Aggregation Behavior

The aggregation of vacancies in alumina crystals drives vacancy migration and redistribution. This study investigates how H proton incorporation alters the vacancy aggregation tendencies in α-Al_2O_3 and θ-Al_2O_3 by analyzing aggregation energy variations (Figures 2–5). Due to structural differences, α-Al_2O_3 contains one type each of Al ($V_{Al\text{-}oct}$) and O (V_O) vacancies, while θ-Al_2O_3 exhibits two Al vacancies ($V_{Al\text{-}oct}$ and $V_{Al\text{-}tet}$) and one O vacancy (V_O).

In the absence of H protons, the vacancy aggregation energies for α-Al_2O_3 are 0.71 eV ($V_{Al\text{-}oct}$) and −0.21 eV (V_O), whereas θ-Al_2O_3 shows values of 1.72 eV ($V_{Al\text{-}oct}$), 0.34 eV ($V_{Al\text{-}tet}$), and −0.07 eV (V_O) (Figures 4 and 5). These results indicate mutual repulsion between V_{Al} vacancies in both phases under natural conditions. The aggregation of Al vacancies in the intrinsic state is thermodynamically unfavorable, which limits Al diffusion via vacancy-mediated mechanisms. Notably, the $V_{Al\text{-}oct}$ aggregation energy in θ-Al_2O_3 is significantly higher than that of $V_{Al\text{-}tet}$ in θ-Al_2O_3 or $V_{Al\text{-}oct}$ in α-Al_2O_3, suggesting that tetrahedral Al vacancies ($V_{Al\text{-}tet}$) are more prone to aggregation. This will provide a low-energy migration pathway for Al atoms from tetrahedral to octahedral sites, thereby facilitating their diffusion. Conversely, V_O vacancies exhibit mutual attraction, with θ-Al_2O_3 displaying a slightly lower aggregation energy (−0.07 eV) than α-Al_2O_3 (−0.21 eV).

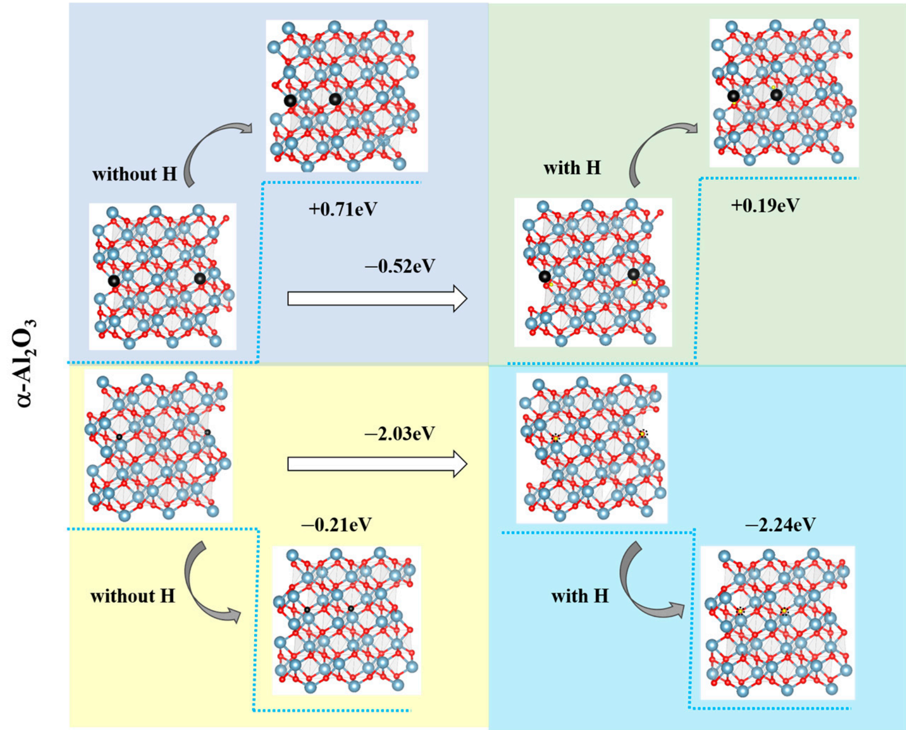

Figure 4. Energy changes in single and double Al/O vacancies in α-Al_2O_3 under undoped and H-doped conditions.

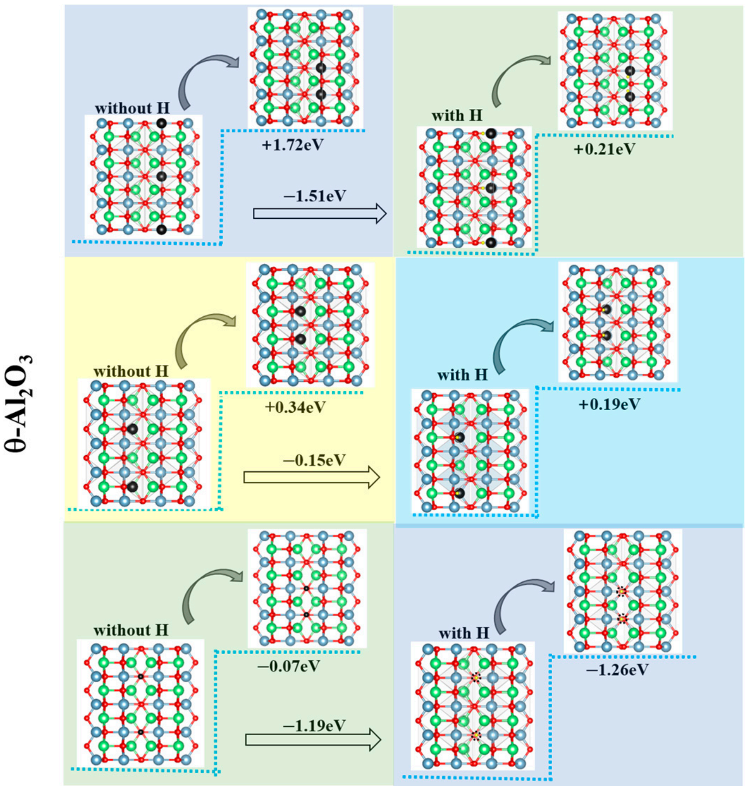

Figure 5. Energy changes in single and double Al/O vacancies in θ-Al_2O_3 under undoped and H-doped conditions.

H proton incorporation markedly reduces vacancy aggregation energies. For α-Al_2O_3, $V_{Al\text{-}oct}$ and V_O energies decrease by 0.52 eV (to 0.19 eV) and 2.03 eV (to −2.24 eV), respectively. In θ-Al_2O_3, reductions of 0.15 eV ($V_{Al\text{-}tet}$), 1.51 eV ($V_{Al\text{-}oct}$), and 1.19 eV (V_O) are observed (Figures 4 and 5). These reductions facilitate vacancy defect generation, particularly for O vacancies, which exhibit greater energy sensitivity than Al vacancies. Upon the introduction of hydrogen protons, the aggregation behavior of oxygen vacancies is significantly enhanced. The aggregation of multiple oxygen vacancies will promote the formation of larger defect clusters, which may further evolve into nanoscale voids within the lattice.

The observed vacancy interactions arise not from classical forces but from charge imbalance effects and electron trapping induced by vacancy formation [38,40]. H protons amplify these interactions, enhancing O vacancy aggregation while weakening Al vacancy repulsion. In α-Al_2O_3 and θ-Al_2O_3, O atoms carry negative charges. O vacancy creation leaves two positive charge centers, promoting attraction to electrons or negatively charged species. H protons increase the positive charge of O vacancies, further driving aggregation. Conversely, Al vacancies generate three negative charge centers due to missing positively charged Al atoms. While these vacancies initially attract positive charges, dominant repulsion from neighboring O ions suppresses aggregation. H proton incorporation mitigates the negative charge of Al vacancies, reducing this repulsion.

3.4. Atomic Migration in Alumina Phases

Extensive research has demonstrated that water vapor critically influences the oxidation dynamics at TBC interfaces, particularly by prolonging the metastable θ-Al_2O_3 phase formation and altering its transition to the stable α-Al_2O_3 phase. This study investigates the mechanistic role of H doping in modulating the migration of Al and O atoms within α-Al_2O_3 and θ-Al_2O_3 supercells. The analysis accounts for two key factors, as follows: (i) during Al migration between octahedral sites, atoms traverse tetrahedral interstitial positions; (ii) oxygen vacancies are introduced during O migration, as H protons preferentially occupy these lattice vacancies.

Figure 6 presents the migration pathways and energy barriers for Al and O atoms in both α-Al_2O_3 and θ-Al_2O_3 phases under H-doped and -undoped conditions. For undoped α-Al_2O_3, the Al and O migration barriers are 1.98 eV ($Al_{107}O_{162}$) and 3.69 eV ($Al_{108}O_{160}$), respectively. The corresponding values for undoped θ-Al_2O_3 are 1.75 eV ($Al_{63}O_{96}$) and 4.25 eV ($Al_{64}O_{94}$). H doping significantly alters these barriers—in α-Al_2O_3, Al migration increases to 3.36 eV ($Al_{107}O_{162}H_1$), while O migration decreases to 2.83 eV ($Al_{108}O_{160}H_1$). Conversely, θ-Al_2O_3 exhibits a dramatic increase in the Al migration barrier to 5.06 eV ($Al_{63}O_{96}H_1$) and a reduction in the O migration barrier to 1.76 eV ($Al_{64}O_{94}H_1$). These correspond to net changes of +1.38 eV (Al) and −0.86 eV (O) in α-Al_2O_3, and of +3.31 eV (Al) and −2.49 eV (O) in θ-Al_2O_3. The results reveal two distinct effects of H doping. Firstly, H doping inhibits Al migration while enhancing O mobility in both phases. This differential behavior arises from proton interactions with charge carriers—H protons increase Coulombic resistance for Al migration but facilitate oxygen ion mobility through vacancy charge redistribution. Secondly, enhanced O migration promotes oxygen vacancy accumulation while suppressing Al vacancy formation. However, excessive H concentrations may saturate oxygen vacancies, paradoxically hindering O migration. The underlying mechanism involves H-induced electronic structure modifications. Proton doping increases the positive charge density at oxygen vacancy sites, attracting negatively charged oxygen ions via Coulombic interactions, thereby reducing their migration barriers. For Al migration, transient H-Al interactions during atomic displacement elevate energy barriers as Al atoms must overcome additional Coulombic forces from localized protons.

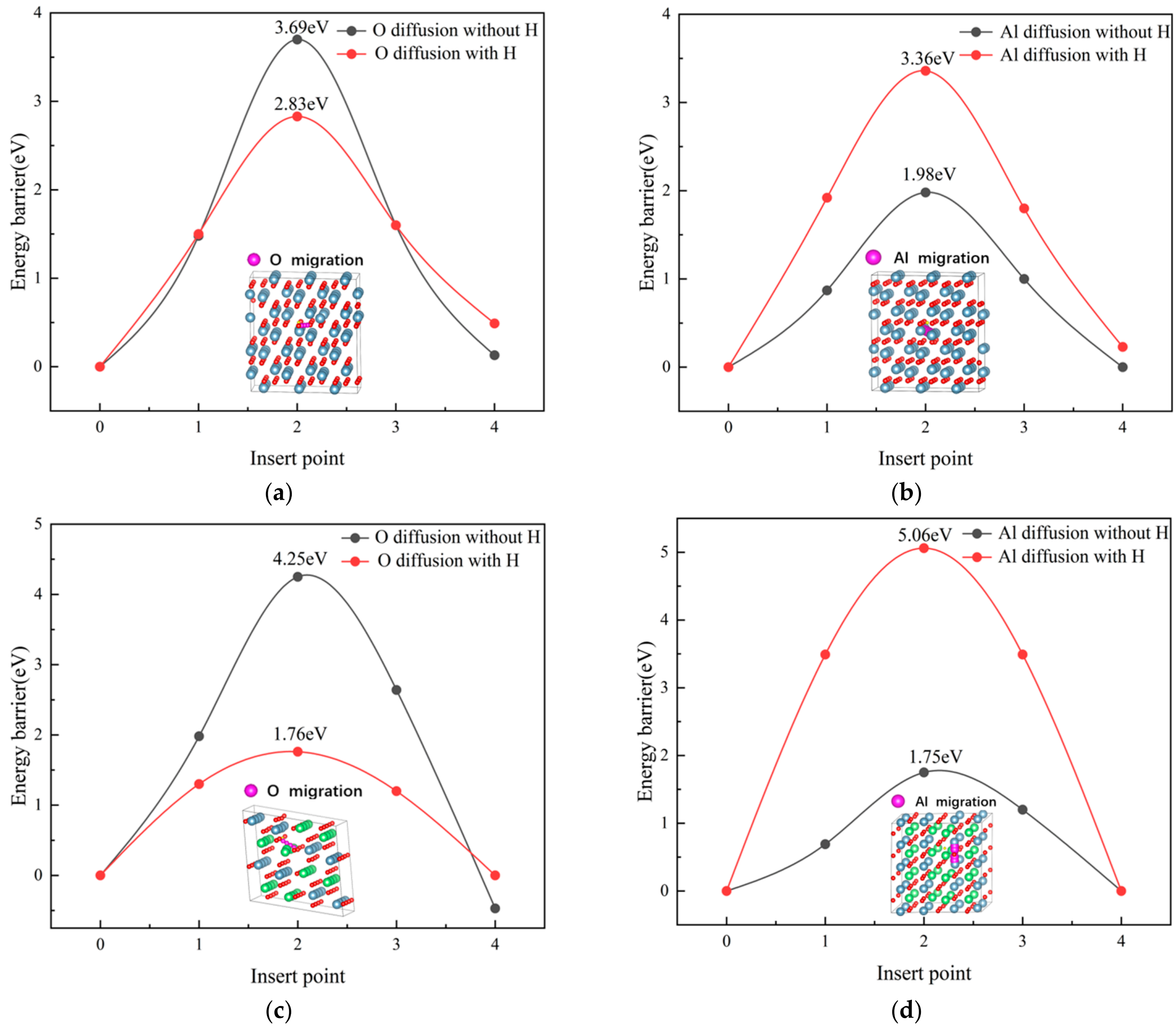

Figure 6. Migration energy barriers and pathways for (**a**) Al and (**b**) O in α-Al_2O_3, as well as (**c**) Al and (**d**) O in θ-Al_2O_3, comparing undoped and H-doped systems.

3.5. Alumina Growth with H Proton Incorporation

The crystal structures of θ-Al_2O_3 and α-Al_2O_3 exhibit distinct differences in the distribution of Al atoms and the arrangement of O sublattices (Figure 1). In θ-Al_2O_3, Al atoms occupy tetrahedral interstitial sites within a face-centered cubic oxygen sublattice, whereas in α-Al_2O_3, Al atoms reside in octahedral interstitial sites within a densely packed hexagonal oxygen sublattice. Early-stage alumina phases (γ, δ) demonstrate oxygen sublattice configurations and Al distributions that are more compatible with θ-Al_2O_3 than with α-Al_2O_3 [11–14]. This structural compatibility reduces nucleation energy barriers and favors lattice matching during initial growth, as the θ-phase requires smaller atomic rearrangements compared to the α-phase. Consequently, θ-Al_2O_3 preferentially forms during the early oxidation stages at TBC interfaces, as illustrated by the lattice structure schematic in Figure 7.

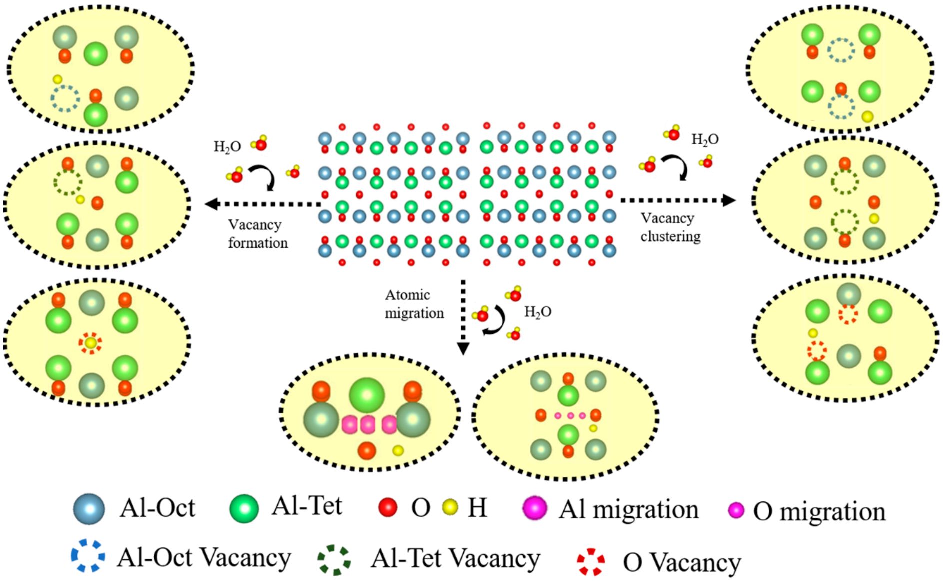

Figure 7. Atomic-scale schematic of H^+ interactions influencing θ-Al_2O_3 lattice growth.

Water vapor exposure facilitates H_2O dissociation into H^+ and OH^- on oxide surfaces, with OH^- further decomposing to release O^{2-} for oxide growth [41–46]. Meanwhile, H^+ diffuses into the oxide lattice, altering vacancy formation and atomic migration (Figure 7). As shown in Table 2, H^+ significantly reduces the Al and O vacancy formation energies in both θ- and α-Al_2O_3. However, θ-Al_2O_3 exhibits lower vacancy formation energies compared to α-Al_2O_3 under H^+ influence, whereby the tetrahedral Al vacancy ($V_{Al\text{-}tet}$) energy in θ-Al_2O_3 is 0.77 eV lower than its octahedral Al vacancy ($V_{Al\text{-}oct}$) energy, as well as being 1.61 eV lower than the $V_{Al\text{-}oct}$ energy in α-Al_2O_3. Similarly, oxygen vacancy (V_O) formation energy in θ-Al_2O_3 is 1.27 eV lower than in α-Al_2O_3. These reductions promote the preferential growth of Al and O vacancies in θ-Al_2O_3, providing abundant migration sites for sustained θ-phase growth while suppressing its transformation to the α-phase. This mechanism aligns with experimental observations of θ-Al_2O_3 stabilization under water vapor environments [26,27].

In the absence of H^+, Al vacancies in α-Al_2O_3 and θ-Al_2O_3 exhibit mutual repulsion, while O vacancies tend to aggregate (Figures 4 and 5). H^+ reduces Al vacancy repulsion and enhances O vacancy aggregation by lowering their respective interaction energies. For Al vacancies, the aggregation energies in θ- and α-Al_2O_3 reduce slightly to 0.21 eV ($V_{Al\text{-}oct}$), 0.19 eV ($V_{Al\text{-}tet}$), and 0.19 eV ($V_{Al\text{-}oct}$) under H^+ influence; however, they remain repulsive, limiting vacancy redistribution. In contrast, the O vacancy aggregation energies decrease sharply to −2.24 eV (α-Al_2O_3) and −1.26 eV (θ-Al_2O_3), promoting vacancy clustering. This disrupts the hexagonal oxygen sublattice in α-Al_2O_3 and induces lattice misalignment, further hindering phase transition. In addition, H^+ preferentially occupies O vacancy sites in both phases (Figure 6), impeding oxygen sublattice shear deformation and reducing Al migration pathways. While H^+ lowers O migration barriers, facilitating O atom mobility and oxide growth, it simultaneously immobilizes near Al vacancies, increasing the Al migration barrier in θ-Al_2O_3 by 1.7 eV compared to α-Al_2O_3. This dual effect stabilizes θ-Al_2O_3 by promoting O-driven growth while restricting the Al rearrangement required for α-phase formation.

4. Concluding Remarks

First-principles calculations were employed to investigate vacancy defect formation, aggregation, and migration in α-Al_2O_3 and θ-Al_2O_3 crystals, with the explicit consideration of hydrogen (H) incorporation from water vapor. Key findings include the following:

1. Hydrogen protons significantly reduce the formation energies of aluminum (Al) and oxygen (O) vacancies in both α-Al_2O_3 and θ-Al_2O_3. This promotes the generation of tetrahedral Al vacancies (VAl-tet), octahedral Al vacancies (VAl-oct), and O vacancies (VO). The resulting local lattice disordering stabilizes metastable alumina phases by mimicking their defect-rich structures, enabling the transient growth of metastable θ-Al_2O_3 under operational conditions.
2. Hydrogen preferentially occupies O vacancy sites in both α-Al_2O_3 and θ-Al_2O_3, while stabilizing near Al vacancies at low-energy configurations. High H concentrations hinder O migration by saturating VO sites, disrupting the oxygen sublattice shear that is required for the θ- to α-Al_2O_3 transition. This inhibits the structural reorganization from a metastable face-centered cubic oxygen arrangement to the thermodynamically stable hexagonal close-packed α-Al_2O_3 structure.
3. Hydrogen enhances the clustering of O vacancies while suppressing repulsion between Al vacancies. Aggregated O vacancies redistribute to form migration pathways for Al and O atoms, sustaining metastable phase growth by expanding oxygen sublattice disorder and defect-mediated Al mobility.
4. Hydrogen suppresses Al migration but accelerates O diffusion in both phases. While enhanced O mobility facilitates metastable phase growth through defect propagation, the inhibition of Al migration prevents structural relaxation into the steady-state α-Al_2O_3 configuration. This kinetic imbalance perpetuates a disordered alumina matrix, favoring prolonged metastability.

These results reveal that hydrogen ingress from water vapor stabilizes metastable θ-Al_2O_3 by amplifying defect generation, altering vacancy dynamics, and disrupting atomic migration, which is critical for phase transitions. These findings provide atomic-scale insights into the degradation mechanisms of thermal barrier coatings in humid environments, establishing a theoretical foundation for the design of hydrogen- and oxidation-resistant coatings via defect engineering and hydrogen mitigation strategies.

Author Contributions: Conceptualization: B.Y. and X.G.; methodology: K.L.; software: K.L.; validation: W.S. and A.A.B.; formal analysis: K.L.; investigation: K.L.; resources: S.S.; data curation: W.S. and A.A.B.; writing—original draft preparation: K.L.; writing—review and editing: S.S., B.Y., and X.G.; supervision: S.S. and X.G.; funding acquisition: B.Y. and X.G. All authors have read and agreed to the published version of the manuscript.

Funding: This work was supported by the National Natural Science Foundation of China (Grant Nos. 52265021 and 52465018), the Specialized Research Fund for the First-Class Disciplines of Education Bureau of Inner Mongolia (No. YLXKZX-NKD-038), and the Central Government in Guidance of Local Science and Technology Development (No. 2022ZY0074).

Institutional Review Board Statement: Not applicable.

Informed Consent Statement: Not applicable.

Data Availability Statement: Data are contained within the article.

Conflicts of Interest: The authors declare no conflicts of interest.

References

1. Clarke, D.R.; Oechsner, M.; Padture, N.P. Thermal-Barrier Coatings for More Efficient Gas-Turbine Engines. *MRS Bull.* **2012**, *37*, 891–898. [CrossRef]
2. Boissonnet, G.; Grégoire, B.; Bonnet, G.; Pedraza, F. Development of Thermal Barrier Coating Systems from Al Microparticles. Part I: Influence of Processing Conditions on the Mechanisms of Formation. *Surf. Coat. Technol.* **2019**, *380*, 125085. [CrossRef]
3. Bo, C.; Jianjun, L.; Guosheng, A.; Wensheng, L.; Xinjiang, Z. Durable Columnar Structure Design for Thermal Barrier Coatings. *Rare Met. Mater. Eng.* **2022**, *51*, 1660–1666.
4. Stefan, E.; Talic, B.; Larring, Y.; Gruber, A.; Peters, T.A. Materials Challenges in Hydrogen-Fuelled Gas Turbines. *Int. Mater. Rev.* **2022**, *67*, 461–486. [CrossRef]
5. Cong, D.; Li, Z.; He, Q.; Chen, H.; Zhao, Z.; Zhang, L.; Wu, H. Wear Behavior of Corroded Al-Al_2O_3 Composite Coatings Prepared by Cold Spray. *Surf. Coat. Technol.* **2017**, *326*, 247–254. [CrossRef]
6. Qiannan, T.A.O.; Yanrong, W.; Dasheng, W.E.I.; Shun, Y. Thermal Oxidation Description Methodology of Thermal Barrier Coatings on Gas Turbine Blades Considering Service Characteristics. *Chin. J. Aeronaut.* **2024**, *37*, 410–424.
7. Mora-García, A.G.; Ruiz-Luna, H.; Alvarado-Orozco, J.M.; Mondragón-Rodríguez, G.C.; Schulz, U.; Muñoz-Saldaña, J. Microstructural Analysis after Furnace Cyclic Testing of Pre-Oxidized ReneN5/(Ni, Pt) Al/7YSZ Thermal Barrier Coatings. *Surf. Coat. Technol.* **2020**, *403*, 126376. [CrossRef]
8. Zhao, W.; Gleeson, B. Assessment of the Detrimental Effects of Steam on Al_2O_3-Scale Establishment. *Oxid. Met.* **2015**, *83*, 607–627. [CrossRef]
9. Jang, S.; Gun Oh, D.; Kim, H.; Hyun Kim, K.; Khivantsev, K.; Kovarik, L.; Hun Kwak, J. Controlling the Phase Transformation of Alumina for Enhanced Stability and Catalytic Properties. *Angew. Chem.* **2024**, *136*, e202400270. [CrossRef]
10. Götlind, H.; Liu, F.; Svensson, J.-E.; Halvarsson, M.; Johansson, L.-G. The Effect of Water Vapor on the Initial Stages of Oxidation of the FeCrAl Alloy Kanthal AF at 900 C. *Oxid. Met.* **2007**, *67*, 251–266. [CrossRef]
11. Rudolph, M.; Salomon, A.; Schmidt, A.; Motylenko, M.; Zienert, T.; Stöcker, H.; Himcinschi, C.; Amirkhanyan, L.; Kortus, J.; Aneziris, C.G. Thermally Induced Formation of Transition Aluminas from Boehmite. *Adv. Eng. Mater.* **2017**, *19*, 1700141. [CrossRef]
12. Busca, G. The Surface of Transitional Aluminas: A Critical Review. *Catal. Today* **2014**, *226*, 2–13. [CrossRef]
13. Kovarik, L.; Bowden, M.; Szanyi, J. High Temperature Transition Aluminas in δ-Al_2O_3/θ-Al_2O_3 Stability Range. *J. Catal.* **2021**, *393*, 357–368. [CrossRef]
14. Kang, S.; Zhao, X.; Guo, J.; Liang, J.; Sun, J.; Yang, Y.; Yang, L.; Liao, R.; Randall, C.A. Thermal-Assisted Cold Sintering Study of Al_2O_3 Ceramics: Enabled with a Soluble γ-Al_2O_3 Intermediate Phase. *J. Eur. Ceram. Soc.* **2023**, *43*, 478–485. [CrossRef]
15. Brumm, M.W.; Grabke, H.J. The Oxidation Behaviour of NiAl-I. Phase Transformations in the Alumina Scale during Oxidation of NiAl and NiAl-Cr Alloys. *Corros. Sci.* **1992**, *33*, 1677–1690. [CrossRef]
16. Chen, Z.; Huang, H.; Zhao, K.; Jia, W.; Fang, L. Influence of Inhomogeneous Thermally Grown Oxide Thickness on Residual Stress Distribution in Thermal Barrier Coating System. *Ceram. Int.* **2018**, *44*, 16937–16946. [CrossRef]
17. Lee, K.N.; Garg, A.; Jennings, W.D. Effects of the Chemistry of Coating and Substrate on the Steam Oxidation Kinetics of Environmental Barrier Coatings for Ceramic Matrix Composites. *J. Eur. Ceram. Soc.* **2021**, *41*, 5675–5685. [CrossRef]
18. Tolpygo, V.K.; Clarke, D.R. Microstructural Study of the Theta-Alpha Transformation in Alumina Scales Formed on Nickel-Aluminides. *Mater. High Temp.* **2000**, *17*, 59–70. [CrossRef]
19. Zhang, X.; Ji, Y.; Chen, L.-Q.; Wang, Y. First-Principles Calculations of γ-Al_2O_3/Al Interfaces. *Acta Mater.* **2023**, *252*, 118786. [CrossRef]
20. Sakakibara, M.; Hanaya, M.; Nakamuro, T.; Nakamura, E. Nondeterministic Dynamics in the η-to-θ Phase Transition of Alumina Nanoparticles. *Science* **2025**, *387*, 522–527. [CrossRef]
21. Alnaeli, M.; Alnajideen, M.; Navaratne, R.; Shi, H.; Czyzewski, P.; Wang, P.; Eckart, S.; Alsaegh, A.; Alnasif, A.; Mashruk, S. High-Temperature Materials for Complex Components in Ammonia/Hydrogen Gas Turbines: A Critical Review. *Energies* **2023**, *16*, 6973. [CrossRef]
22. Chen, K.; Seo, D.; Canteenwalla, P. The Effect of High-Temperature Water Vapour on Degradation and Failure of Hot Section Components of Gas Turbine Engines. *Coatings* **2021**, *11*, 1061. [CrossRef]
23. Brossard, M.; Bouchaud, B.; Pedraza, F. Influence of Water Vapour on the Oxidation Behaviour of a Conventional Aluminide and a New Thermal Barrier Coating System Sintered from a Slurry. *Mater. Corros.* **2014**, *65*, 161–168. [CrossRef]
24. Allo, J.; Jouen, S.; Roussel, M.; Gibouin, D.; Sauvage, X. Influence of Sulfur and Water Vapor on High-Temperature Oxidation Resistance of an Alumina-Forming Austenitic Alloy. *Oxid. Met.* **2021**, *95*, 359–376. [CrossRef]
25. Yan, K.; Guo, H.; Gong, S. High-Temperature Oxidation Behavior of Minor Hf Doped NiAl Alloy in Dry and Humid Atmospheres. *Corros. Sci.* **2013**, *75*, 337–344. [CrossRef]
26. Zhu, D.; Wang, X.; Zhao, J.; Lu, J.; Zhou, Y.; Cai, C.; Huang, J.; Zhou, G. Effect of Water Vapor on High-Temperature Oxidation of NiAl Alloy. *Corros. Sci.* **2020**, *177*, 108963. [CrossRef]

27. Cheng, Y.; Li, C.; Yuan, X.; Huang, T.; Song, P. The Role of High-Temperature Water Vapor on Oxidation Behavior for CoNiCrAlHf Alloys at 1100 °C. *Mater. Charact.* **2024**, *210*, 113829. [CrossRef]
28. Bagwell, R.B.; Messing, G.L.; Howell, P.R. The Formation of α-Al_2O_3 from θ-Al_2O_3: The Relevance of a "Critical Size" and: Diffusional Nucleation or "Synchro-Shear"? *J. Mater. Sci.* **2001**, *36*, 1833–1841. [CrossRef]
29. Huang, Y.; Peng, X.; Chen, X.-Q. The Mechanism of θ-to α-Al_2O_3 Phase Transformation. *J. Alloys Compd.* **2021**, *863*, 158666. [CrossRef]
30. Ru, Q.; Qiu, X.L. The Electronic Structure and Mechanical Property of Alpha Al_2O_3 by First Principles Calculation. *Mater Res Appl.* **2009**, *3*, 162–167.
31. Wang, X.-L.; Hubbard, C.R.; Alexander, K.B.; Becher, P.F.; Fernandez-Baca, J.A.; Spooner, S. Neutron Diffraction Measurements of the Residual Stresses in Al_2O_3-ZrO_2 (CeO_2) Ceramic Composites. *J. Am. Ceram. Soc.* **1994**, *77*, 1569–1575. [CrossRef]
32. Ishizawa, N.; Miyata, T.; Minato, I.; Marumo, F.; Iwai, S. A Structural Investigation of α-Al_2O_3 at 2170 K. *Struct. Sci.* **1980**, *36*, 228–230. [CrossRef]
33. Husson, E.; Repelin, Y. Structural Studies of Transition Aluminas. Theta Alumina. *Eur. J. Solid State Inorg. Chem.* **1996**, *33*, 1223–1231.
34. Zhang, G.; Xiang, X.; Yang, F.; Peng, X.; Tang, T.; Shi, Y.; Wang, X. Helium Stability and Its Interaction with H in α-Al_2O_3: A First-Principles Study. *Phys. Chem. Chem. Phys.* **2016**, *18*, 1649–1656. [CrossRef] [PubMed]
35. Zhang, G.; Lu, Y.; Wang, X. Hydrogen Interactions with Intrinsic Point Defects in Hydrogen Permeation Barrier of α-Al_2O_3: A First-Principles Study. *Phys. Chem. Chem. Phys.* **2014**, *16*, 17523–17530. [CrossRef]
36. Zhou, H.; Ji, Y.; Wang, Y.; Feng, K.; Luan, B.; Zhang, X.; Chen, L.-Q. First-Principles Lattice Dynamics and Thermodynamic Properties of α-, θ-, κ-and γ-Al_2O_3 and Solid State Temperature-Pressure Phase Diagram. *Acta Mater.* **2024**, *263*, 119513. [CrossRef]
37. Lei, Y.; Gong, Y.; Duan, Z.; Wang, G. Density Functional Calculation of Activation Energies for Lattice and Grain Boundary Diffusion in Alumina. *Phys. Rev. B—Condens. Matter Mater. Phys.* **2013**, *87*, 214105. [CrossRef]
38. Lei, Y.; Wang, G. Linking Diffusion Kinetics to Defect Electronic Structure in Metal Oxides: Charge-Dependent Vacancy Diffusion in Alumina. *Scr. Mater.* **2015**, *101*, 20–23. [CrossRef]
39. Hinuma, Y.; Kamachi, T.; Hamamoto, N.; Takao, M.; Toyao, T.; Shimizu, K. Surface Oxygen Vacancy Formation Energy Calculations in 34 Orientations of β-Ga_2O_3 and θ-Al_2O_3. *J. Phys. Chem. C* **2020**, *124*, 10509–10522. [CrossRef]
40. He, Q.; Liu, D.; Zhou, Y.; Sun, T.-Y.; Huang, L.-F. Nitride Coatings for Environmental Barriers: The Key Microscopic Mechanisms and Momentous Applications of First-Principles Calculations. *Surf. Sci. Technol.* **2024**, *2*, 24. [CrossRef]
41. Henderson, M.A. The Interaction of Water with Solid Surfaces: Fundamental Aspects Revisited. *Surf. Sci. Rep.* **2002**, *46*, 1–308. [CrossRef]
42. Salmeron, M.; Bluhm, H.; Tatarkhanov, M.; Ketteler, G.; Shimizu, T.K.; Mugarza, A.; Deng, X.; Herranz, T.; Yamamoto, S.; Nilsson, A. Water Growth on Metals and Oxides: Binding, Dissociation and Role of Hydroxyl Groups. *Faraday Discuss.* **2009**, *141*, 221–229. [CrossRef]
43. Chen, X.; Shan, W.; Wu, D.; Patel, S.B.; Cai, N.; Li, C.; Ye, S.; Liu, Z.; Hwang, S.; Zakharov, D.N. Atomistic Mechanisms of Water Vapor–Induced Surface Passivation. *Sci. Adv.* **2023**, *9*, eadh5565. [CrossRef] [PubMed]
44. Xiang, X.; Yang, F.; Hu, L.; Zhang, G.; Chen, C. The Role of Carbon in the Formation of Intrinsic Point Defects and Hydrogen Migration in α-Al_2O_3-Based Tritium Permeation Barriers. *Phys. Status Solidi B* **2022**, *259*, 2200284. [CrossRef]
45. Li, H.; Zhao, X.; Zhang, H.; Li, J.; Li, D. High-Temperature Oxidation of 60Si2Mn Spring Steel in Dry Air and Wet Air: Insights from an Experimental and First-Principles Study. *Steel Res. Int.* **2023**, *94*, 2200691. [CrossRef]
46. Luo, L.; Su, M.; Yan, P.; Zou, L.; Schreiber, D.K.; Baer, D.R.; Zhu, Z.; Zhou, G.; Wang, Y.; Bruemmer, S.M. Atomic Origins of Water-Vapour-Promoted Alloy Oxidation. *Nat. Mater.* **2018**, *17*, 514–518. [CrossRef]